LAWRENCE
LIVERMORE
NATIONAL
LABORATORY

LLNL-TR-692285

Dynamic Fracture Simulations of Explosively Loaded Cylinders

C. W. Arthur, D. M. Goto

May 17, 2016

Disclaimer

This work performed under the auspices of the U.S. Department of Energy by Lawrence Livermore National Laboratory under Contract DE-AC52-07NA27344.

Dynamic Fracture Simulations of Explosively Loaded Cylinders

Department of Civil and Environmental Engineering
University of California, Davis

Carly W. Arthur, MS Student in Structural Engineering

11/30/2015

This work was performed under the auspices of the U.S. Department of Energy by Lawrence Livermore National Laboratory under Subcontract B611893.

Table of Contents

Table of Tables

Table of Equations

Table of Figures

Introduction

This report documents the modeling results of high explosive experiments investigating dynamic fracture of steel (AerMet® 100 alloy) cylinders. The experiments were conducted at Lawrence Livermore National Laboratory (LLNL) during 2007 to 2008 [10]. A principal objective of this study was to gain an understanding of dynamic material failure through the analysis of hydrodynamic computer code simulations. Two-dimensional and three-dimensional computational cylinder models were analyzed using the ALE3D multi-physics computer code.

Cylinder Experiment

Materials

The experiments used hollow cylinders machined from AerMet® 100 steel alloy. AerMet® 100 steel is an alloy possessing high hardness and strength combined with exceptional ductility and toughness [1]. High strain-rate loading (~50, 000/s) of the steel was achieved by using Livermore Explosive 17 (LX-17), which is characterized by its dramatic insensitivity to mechanical stimuli [4]. The LX-17 main charge was placed and subsequently detonated inside the hollow steel cylinder. Detonation initiation of the LX-17 main charge was achieved by using a RP-1 detonator to ignite a conventional high explosive frustum of Livermore Explosive 10 (LX-10). The insensitive nature of LX-17 requires a LX-10 booster to be used in conjunction with a detonator to properly initiate detonation. Igniting the LX-17 high explosive with the LX-10 booster provides a near planar detonation to the main charge. The LX-17 high explosive was bonded or fixed to the steel using APC2.5 (silastic), which is a flexible, inert silicone elastomer [5].

Geometry

The hollow steel cylinder geometry is described in [10] and restated here for reference. The outer diameter of the AerMet® 100 steel cylinder is 50.8 mm, with a wall thickness of 3 mm and a nominal length of 203.2 mm. A solid cylinder of LX-17 high explosive, approximately 600.5 g, is placed inside the hollow steel cylinder. A 42.2 g frustum of LX-10 booster charge is fixed to one end of the LX-17 solid cylinder. The RP-1 detonator is centered on the LX-10 frustum and used to ignite the booster charge.

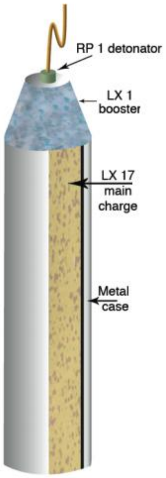

Figure 1 - Schematic of cylinder experiment [10].

Measured Data

High Speed Camera Images & Radiographs

High-speed digital framing cameras captured the evolution of the high explosive detonation, (cylinder) steel expansion and fracture behavior. Figure 2 shows an optical image 21 μs after detonation is fired; the RP-1 detonator and booster are located at the top of the image. The camera image exhibits the range of deformation history experienced by the steel, including the un-deformed material (bottom) to completely fractured and fragmented (top). X-ray radiographs illustrate the fracture pattern characteristics shown in Figure 2 [10].

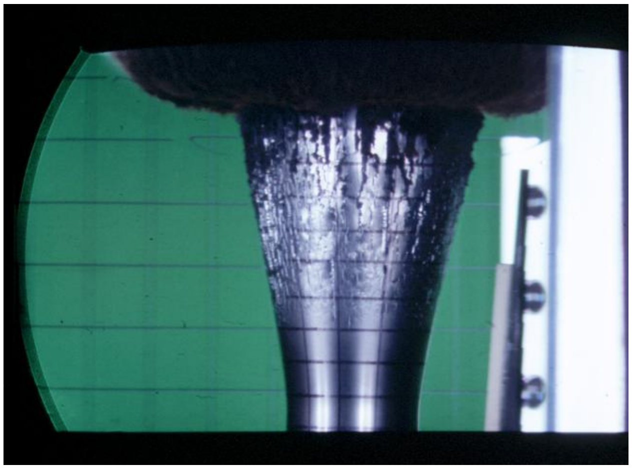

Figure 2 - Optical image of exploding AerMet® 100 alloy cylinder approximately 21 μs after detonation [10].

Velocimetry

Laser interferometry was used to measure the expansion velocity of the steel cylinder. Utilizing fiber optic probes, laser light was focused on the outer steel surface. The probes were located along the length of the cylinder at 38.1 mm (P1), 76.2 mm (P2), 114.3 mm (P3) and 152.4 mm (P4), measured from the top of the cylinder, where the detonation initiates.

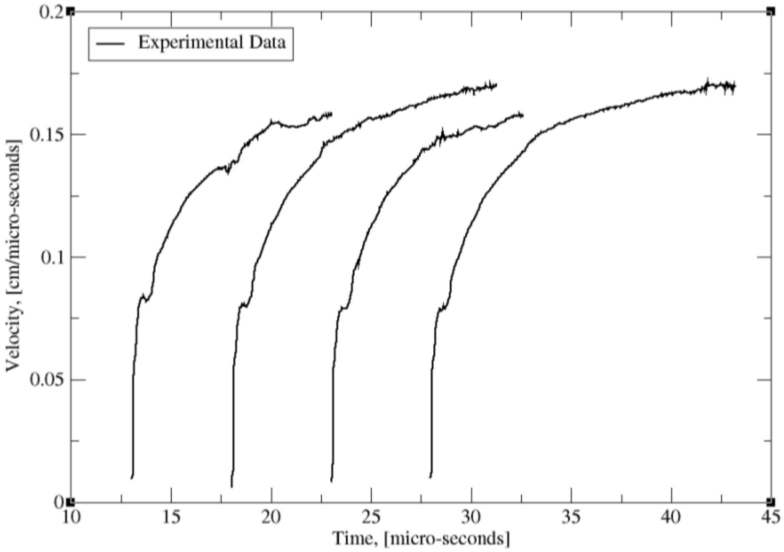

Figure 3 - Experimentally measured AerMet® 100 steel cylinder expansion velocity, with the first curve representing the closest probe to the detonated end of the cylinder (at 38.1 mm).

Strain to Failure

A soft capture apparatus [10] was utilized to recover AerMet® 100 steel fragments after detonation of the cylinder experiment. The thickness of each recovered fragment was measured in three different locations. From the thickness measurements, the logarithmic through-thickness strain was computed, assuming:

$$\varepsilon_{tt} = -\ln\left(\frac{t_{final}}{t_{initial}}\right) \qquad (1)$$

where t_{inital} and t_{final} are the initial and final thickness of the steel casing, respectively. The strain at which failure occurred or the net equivalent plastic strain (EPS) can be defined as [13]:

$$\bar{\varepsilon} = \sqrt{\frac{2}{9}[(\varepsilon_1 - \varepsilon_2)^2 + (\varepsilon_2 - \varepsilon_3)^2 + (\varepsilon_3 - \varepsilon_1)^2]} \qquad (2)$$

If we assume the cylinder was loaded under plane strain conditions, $\varepsilon_1 = -\varepsilon_2\,, \varepsilon_3 = 0$, the strain at which failure occurred, can be derived as:

$$\bar{\varepsilon} = \sqrt{\frac{2}{9}[(\varepsilon_1 - (-\varepsilon_1))^2 + (-\varepsilon_1 - 0)^2 + (0 - \varepsilon_1)^2]} = \bar{\varepsilon} = \sqrt{\frac{2}{9}[6\varepsilon_1^2]} = \frac{\mathbf{2}}{\sqrt{\mathbf{3}}}\boldsymbol{\varepsilon_{tt}}$$

The failure strains of the experiment were computed using the analytical results above and graphically presented in Figure 4.

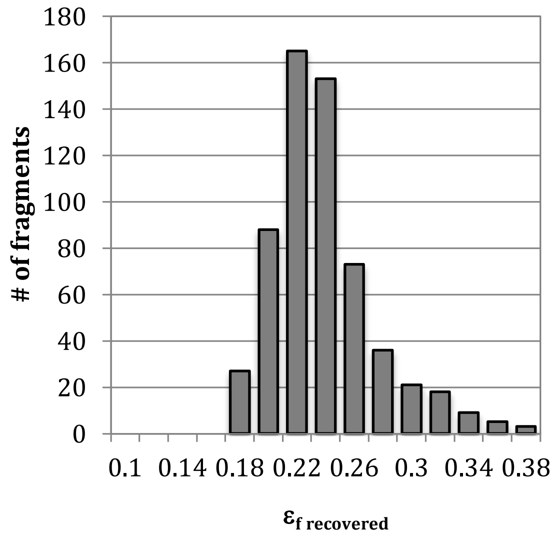

Figure 4 - Strain to failure distribution measured from the recovered steel fragments, using 10% bins.

As observed from Figure 4, the experimentally measured failure strains exhibit statistical variation with arithmetic average of 0.229 and a median of 0.223. This behavior can be characterized by common probability distribution functions, such as Weibull and Gaussian.

Computational Modeling

Using discretized simulation models, computational code simulations were calculated to analyze the dynamic fracture and failure of the steel cylinder. A multi-physics computer code, ALE3D, was utilized to generate and perform the computational simulations. The calculations use a hybrid methodology of both finite element and finite volume formulation on an unstructured grid to model the fluid and elastic-plastic response [18] of a metal cylinder loaded with high explosive. A combination of Lagrangian and Eulerian methodologies with mesh relaxation was used to model deformation and fracture behavior of the steel cylinder (further explanation in later sections). A constitutive yield strength and flow stress (hardening) model, an equation of state (for the steel and high explosive materials) and a statistics compensated failure model were also utilized to define the material response. The calibration of the material models available in ALE3D was achieved through the analysis of experimental data. Materials Science Database (MSD) and Material Implementation, Database and Analysis Source (MIDAS) [6] were utilized for the material model approximations derived from available AerMet® 100 steel data.

Constitutive (Material) Model for AerMet® 100 Steel

A constitutive model describes the strength and hardening response of the steel material. The Steinberg-Guinan strength model is a rate and temperature independent (rate insensitive) yield strength and strain-hardening model with a temperature and pressure dependent shear modulus [2]. The Steinberg-Guinan strength model is defined as [16]:

$$Y = Y_0[1 + \beta(\varepsilon + \epsilon_i)^n]\frac{G}{G_0} \qquad (3)$$

where Y is the current flow stress, Y_0 is the yield strength at $\varepsilon = 0$, ϵ is the plastic strain, β is a strength parameter, n is the work-hardening exponent, and G/G_0 is a normalized shear modulus. The Steinberg-Guinan shear modulus, G, is defined as [2]:

$$G = \left[G_0 + a_P G_0 P\left(1 - a_n + a_n \eta^{-\frac{1}{3}}\right) - G_0 a_T\left(T - T_{ref}\right)\right]\exp\left(-\frac{a_M E}{E_m - E}\right), \eta = \frac{\rho}{\rho_0} \qquad (4)$$

where E is Young's modulus, G_0 is the shear modulus, a_P represents the pressure dependence on G, a_n is the relative volume dependence of G, a_T is the linear temperature dependence, a_M is the coefficient to adjust the melt-softening and T_{ref} is the reference temperature. Strength model parameters were determined by model calibration to experimental stress strain data, which was measured at room temperature (298 K), at strain-rates between 0.001/s and 2500/s, and plastic strains up to 0.30 (30%). Parameters for the temperature and pressure dependent shear modulus were assumed to be similar to Vascomax 250 steel [2]. The parameters were calibrated using a fitting method similar to least squares, to optimize the model agreement to the experimental data.

Equation of State (Material) Model for AerMet® 100 Steel

The Mie-Grüneisen equation of state model is an analytic model, which characterizes the pressure-volume-energy (P-V-E) relationship [2]:

$$P = \begin{cases} \dfrac{\rho_0 c^2 \mu\left[1+\left(1+\frac{\gamma_0}{2}\right)\mu-\frac{a}{2}\mu^2\right]}{\left[1-(S_1-1)\mu-S_2\frac{\mu^2}{(\mu+1)}-S_3\frac{\mu^3}{(\mu+1)^2}\right]^2} + (\gamma_o + a\mu)E, & for\ \mu > 0 \\ \rho_0 c^2 \mu + (\gamma_0 + a\mu)E, & for\ \mu < 0 \end{cases} \qquad (5)$$

where $\rho_0 c^2$ is the bulk modulus, a is the linear correction to γ_0 (reference Grüneisen gamma) and S_1 is the linear coefficient of the shock speed for particle speed relation, S_2 is the quadratic coefficient and S_3 is the cubic coefficient. S_1 was calibrated to be 1.33 while S_2 and S_3 were taken to be zero. Model parameters used for the AerMet® 100 steel are derived from Vascomax 250 steel [2], and obtained from shock Hugoniot experiments. The volumetric compression is given as $\mu = \frac{\rho}{\rho_0} - 1 = \eta - 1$. A cold curve (not shown), which can be considered as a pressure volume relation at a 0 K reference state, and a melt curve (not shown), which characterizes the conditions under which the material is melted, were also used and assumed to be identical to Vascomax 250 steel [2].

Equation of State (Material) Model for High Explosives

A reacted product equation of state, Jones-Wilkins-Lee (JWL) model, was used to describe the volumetric response of the LX-17 and LX-10 high explosives. The JWL model is an analytic representation of the pressure-volume-energy relationship for the expanding (reacted) high explosive gas products. Model parameters used for LX-17 and LX-10 were derived from [4]. The JWL equation of state is defined in [2] as:

$$P = A\left(1 - \frac{\omega}{R_1 \nu}\right)\exp(-R_1 \nu) + B\left(1 - \frac{\omega}{R_2 \nu}\right)\exp(-R_2 \nu) + \frac{\omega}{\nu} e \qquad (6)$$

where ν is the relative volume ($\nu = \frac{V}{V_0} = \frac{\rho_0}{\rho}$). The parameters of A, B, R_1, R_2 and ω are material dependent parameters used to define the JWL equation of state and are calculated based on specialized Copper cylinder expansion tests [8, 10]. The JWL parameters utilized are tabulated in [4] and restated here for reference:

Table 1 - JWL equation of state parameters for LX-10 (booster) and LX-17 (main charge).

	A	B	R_1	R_2	ω
LX-10	7.132	0.149436	4.25	1.25	0.25
LX-17	4.603	0.095518	4.00	1.70	0.48

Burn Models for High Explosive Behavior

In addition to the equation of state model (JWL), a detonation propagation model (burn model) is also required to describe the high explosive response of LX-17 and LX-10. The explosive propagation (burn) model represents the high explosive rate of reaction and is a function of the high explosive's detonation velocity. The burn model used for LX-10 is a programmed lighting time model (program burn model). The (burn) model is initiated by igniting a point at the center of the top surface of the booster. The LX-10 program burn model uses the detonation velocity (8.82 mm/µs) to calculate the time at which a zone will detonate. Detonation of the zone is represented by a rapid release of high explosive energy. Once the (lighting) time for a zone is reached, the energy is released, causing the pressure to increase. This action activates the JWL equation of state, thusly simulating detonation in the LX-10 high explosive. The LX-17 detonation is initiated using a compression based burn model. The augmented beta burn model relates a parameter, beta (β), to the equation of state (JWL) and the detonation velocity of LX-17 (7.596 mm/µs) [2]:

$$\beta = \frac{1}{1-\frac{v_{CJ}}{v_\beta}} \tag{7}$$

where v_{CJ} is the Chapman-Jouget relative volume and v_β is the reference relative volume. The beta burn fraction is then defined as [2]:

$$f_\beta = \beta(1 - \frac{v}{v_\beta}) \tag{8}$$

where v is the relative volume. An augmented beta burn is calculated when the actual burn fraction of a zone exceeds the lighting threshold (specified to be 50%) by treating each zone as a detonator. The treatment of each zone as a detonator ensures the propagation of the detonation through the LX-17 main charge.

Failure (Material) Model for AerMet® 100 Steel

A Johnson-Cook failure model was calibrated as the failure mechanism of the computational simulations. The Johnson-Cook failure model is defined by scalar damage parameters:

$$D = \sum \frac{\dot{\varepsilon^p} \Delta t}{\varepsilon_f} \tag{9}$$

where Δt is the time step, $\dot{\varepsilon}^p$ is the equivalent plastic strain rate and ε_f is the failure strain calculated by the Johnson-Cook failure model [13]:

$$\varepsilon^f = [D_1 + D_2 \exp(-D_3 \frac{\sigma_m}{\bar{\sigma}})] * [1 + D_4 \ln \frac{\dot{\varepsilon}}{s^{-1}}] * [1 + D_5 T^*] \tag{10}$$

The material is presumed to fail when damage (equation 9) reaches unity ($D = 1.0$). The first bracketed expression in equation 10 describes the effect of stress triaxiality with the D_3 damage parameter generalized by Hancock-McKenzie to be equal to 1.5, assuming spherical void growth [13, 14]. Because the experiment was conducted at equivalent strain rates and ambient (room) temperature, the strain rate and temperature terms which involved D_4 and D_5 were neglected (effectively set to zero for this study) [10]. Furthermore, to simplify the material modeling, D_1 was set to zero [8]. Thusly, a simplified Johnson-Cook failure model was utilized:

$$\varepsilon^f = D_2 \exp\left(-D_3 \frac{\sigma_m}{\bar{\sigma}}\right) \tag{11}$$

Applying Statistical Compensation to the Johnson-Cook Failure Model

Inherent statistical variation is observed in material fracture and fragmentation. The experimental strain to failure measurements of the recovered AerMet® 100 steel fragments characterize this statistical behavior. To accurately capture the dynamic material failure of the steel, the Johnson-Cook failure model was modified to accommodate material (damage) parameters that could be defined as statistical quantities. The simplified Johnson-Cook failure model utilized (equation 11) is defined by the damage parameter, D_2, which scales the nominal failure surface (D_1 provided a vertical translational shift). The damage parameter, D_2, can be defined as a statistical quantity to provide statistical randomness to the steel failure. Therefore, equation 11 becomes:

$$\varepsilon^f = f_{\varepsilon-fail} \exp\left(-D_3 \frac{\sigma_m}{\bar{\sigma}}\right) \tag{12}$$

where, $f_{\varepsilon-fail}$ is represented by a Weibull distribution. From [10] and commonly used in failure analysis; a Weibull probability distribution function represents the statistical variation in the measured failure strains (refer to Figure 4). A standard three-parameter Weibull probability distribution function is expressed as [1, 5]:

$$f_{\varepsilon-fail} = \left(\frac{\beta}{\eta}\right)\left(\frac{\varepsilon-\varepsilon_0}{\eta}\right)^{\beta-1} \exp[-\left(\frac{\varepsilon-\varepsilon_0}{\eta}\right)^{\beta}] \tag{13}$$

where ε is the strain to failure (expressed in terms of the equivalent plastic strain), β is the shape parameter and η is the scale parameter. The third parameter, ε_0, is defined as a threshold, below which there is (effectively) zero probability the material will fail. It is common for β to be greater than one as this is indicative of the failure rate increasing with time [17]. For a β less than 2.7, the Weibull distribution is skewed-right and for a β greater than 3.7, the Weibull distribution is skewed-left [17]. In order to fit the analyzed strain to failure of the recovered cylinder fragments, a Weibull distribution is defined by the following parameters.

Table 2 - Weibull parameters determined based on recovered fragments from an AerMet® 100 steel alloy cylinder [10].

	β	η	ε_0
AerMet® alloy cylinder [10]	2	0.065	0.165

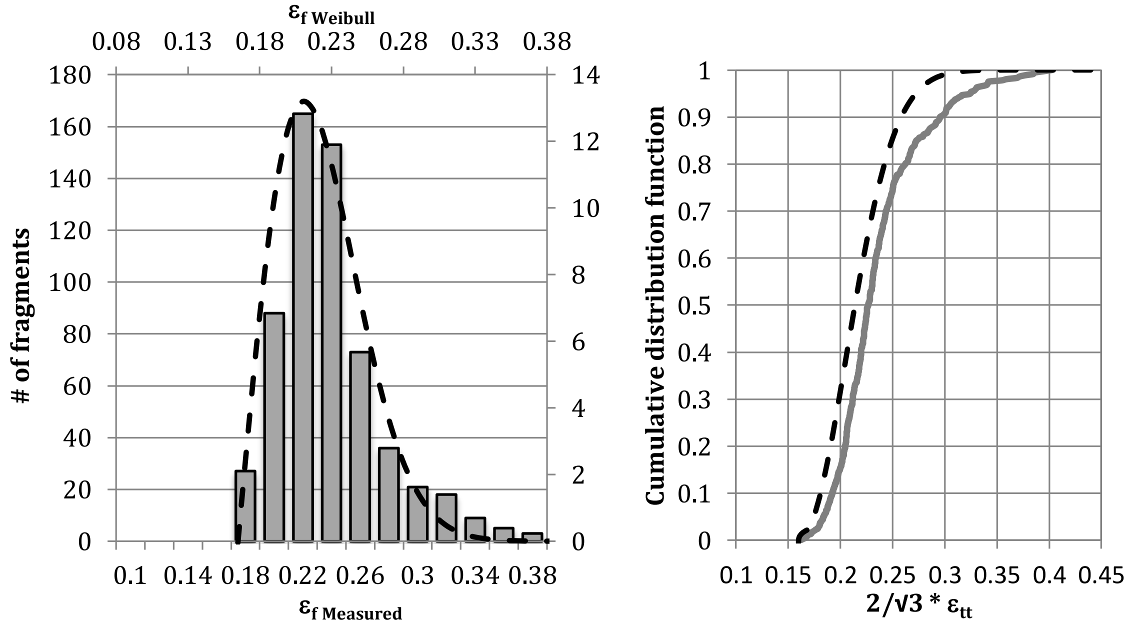

Figure 5 - Superimposed on experimentally measured failure strain histogram from Figure 4 (left) [10] and integrated normalized failure strains (right) is a Weibull probability distribution function (left) and cumulative distribution function (right) that has been normalized to the number of fragments from the cylinder experiment.

The failure strains of the recovered fragments are integrated and normalized to produce a cumulative distribution function of failure strains (Figure 5, right, gray solid line). The cumulative Weibull distribution represents the measured (integrated) failure strains from the recovered steel fragments (Figure 5, right, black dotted line). ALE3D will sample the input Weibull cumulative distribution function between zero and one and populate a steel zone (mesh element) with the corresponding failure strain (D_2) value. This process will be repeated until all the zones are seeded with statistic Weibull (D_2) failure strains. This generates a random distribution of failure strains for the steel cylinder. When parallel computing is used, a random distribution of failure strains for each processor is generated to ensure complete randomness.

ALE3D Models

The ALE3D computational modeling of the steel cylinder was performed using two different computer code approaches, which are referred to here as "ALE" and "embedded grid". Both approaches utilize a Johnson-Cook failure model and its associated damage evolution rule to initiate “fracture” or material separation into the steel. The ALE approach used a technique referred to as “void seeding” in order to model material separation (fracture), whereas the embedded grid approach used a technique referred to as “element erosion”.

ALE Calculations with Void Seeding and Slide Surfaces

The arbitrary Lagragian-Eulerian (ALE) is a finite element formulation constructed of a combination of Lagrangian and Eulerian steps. Traditional Lagrangian formulation is defined as the material is attached to and moves with the computational mesh. Traditional Eulerian formulation is defined as the material moves through the computational mesh (mesh is spatially fixed). In ALE calculations, the computational mesh within the boundaries can move arbitrarily to optimize the shape of the elements (Eulerian formulation), while the mesh defined on the boundaries can move with the material (Lagrangian formulation) to preserve distinct material interfaces. Large mesh distortions are addressed with the use of ALE and its advection techniques. Advection is defined as the process for modifying the existing mesh (relax the mesh) to alleviate Lagrangian tangling or preserve an Eulerian grid [2]. During the relaxation step, the mesh is allowed to cross material boundaries and multiple material (mixed) zones are created. State variables are transferred from the original mesh to the modified mesh after each Lagrangian step.

For accurate modeling of the steel and high explosive interface, a slide surface was specified between the silastic outer diameter and the inner steel surface (at a radius of 24.6 mm). Specific to the ALE calculations, slide surfaces are a numerical technique which models contact discontinuities [2]. This specification facilitates accurate calculations of the dynamic steel behavior as the detonation shock traverses the inside surface of the steel casing. The zones of each material (silastic and steel) move with respect to one another instead of the steel zones dramatically distorting as a result of the dynamic loading conditions of the problem (LX-17 detonation).

Finite-volume void seeding introduces material failure initiation into the computational mesh by the insertion of voids into steel zones. The definition of a void material is one that maintains constant density and pressure. It is used to model low-density gas or empty space [2] and is defined by having no constitutive material response. Finite-volume void seeding is triggered when the relative volume exceeds a relative volume threshold (1.03 is currently utilized). Failure (accumulated Johnson-Cook damage = 1.0) and exceeding the relative volume threshold of a steel zone must be satisfied before void is inserted. Based on the 1.03 relative volume threshold, the internal composition is now defined as a mixed zone with volume fractions of 3% void and 97% steel. The insertion of void will reset the damage parameter to 0.85 and resume Johnson-Cook failure model evaluations (i.e., the zone is set to be un-failed). The volumetric (principal) strain is partitioned to the void while the deviatoric (shear) strain is represented in the steel. Within the mixed zone formulation, the void is allowed to expand throughout the duration of the simulation until it is advected away leaving behind a separation between adjacent steel zones or a "crack".

Embedded Grid Calculations with Element Erosion

The embedded grid approach is defined by the specification of a foreground and background mesh. The foreground mesh consists entirely of the steel cylinder, which is modeled "conformally" (mesh elements align with geometric boundaries). The steel is modeled Lagrange for the entire duration of the simulation, which means the ALE formulation and specifically advection (mesh relaxation) is not utilized. Lagrangian movement is a very accurate method to calculate dynamic behavior of the steel cylinder. The background mesh comprises all other materials specified in the problem: LX-10, LX-17, silastic, air and void. It behaves similarly to the previously defined ALE calculations. The specifications of two meshes (foreground and background) allow for independent movement and the mesh size can be refined separately. Figure 6 visualizes how the steel foreground mesh (gray) overlays the background mesh. Note that the steel mesh zones (gray) do not align with the air zones (light blue).

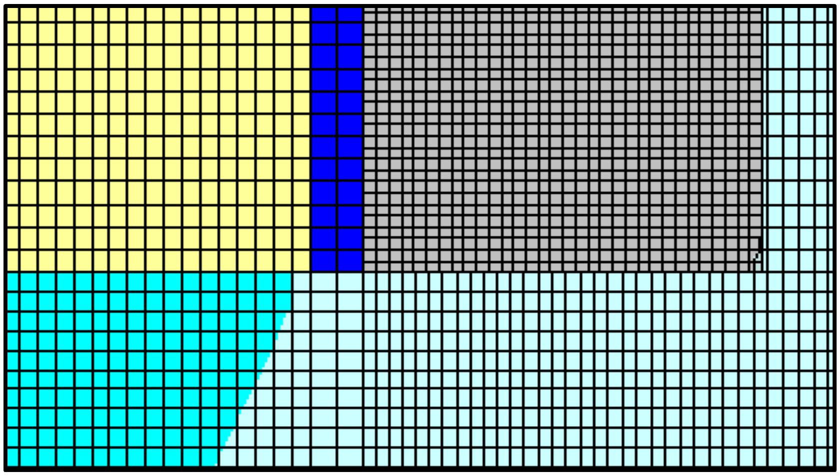

Figure 6 - 2D simulation image of foreground steel mesh (gray) overlaying ALE background mesh (light blue is air, light yellow is LX-10, dark blue is silastic and cyan is LX-10) for the specification of the embedded grid computational mesh. Note how the steel zones (gray) do not align with the air zones (light blue).

The embedded grid methodology utilizes element erosion for material failure initiation into the computational mesh, which is the deletion of zones (mesh elements) based on user-defined criteria. This implementation completely removes eroded elements from the calculation. It is controlled by the specification of rules or restrictions on parameters or variables that must be satisfied before the element is allowed to erode. The rules utilized are accumulated damage and distortion of the mesh elements. Only when an element is distorted to 95% of its original mapping and the element's accumulated damage equates to 98% is the element allowed to erode and therefore is deleted from the calculation. The nodes of each eroded element retain the mass contribution if that element meets the specified criteria to be deleted. If all elements associated with a node meet the criteria for erosion, the current mass of the node (associated with the eroded elements) is consequently deleted.

Discretized Computational Model (Mesh)

The three-dimensional computational mesh is a hollow steel cylinder filled with high explosive. Although the original experiment was designed to be two-dimensional [10], three-dimensional modeling is required to study dynamic fracture. The cylinder configuration was modeled as the LX-17 high explosive core, silastic potting compound between the steel and explosive (to ensure no air between the LX-17 and steel zones), the hollow steel cylinder and air. These geometric components are modeled "conformally", or the specification that all mesh elements conform to geometric boundaries (i.e. distinct material interfaces are present). This ensures accurate calculations of the steel's dynamic behavior. Modeling the air allows the expansion of the fragmented steel, while preventing excessive steel mesh distortion. The air is zoned by a ratio that ensures finer mesh resolution near the outside surface of the steel. As the radius approaches 120 mm, the mesh elements will uniformly increase in size. The LX-17 high explosive core was modeled as a cylinder with 320 mesh elements spanning the 44.0 mm diameter. The steel cylinder was modeled by 16 zones across the 3 mm thickness dimension (5.3 zones/mm). The thin silastic layer between the LX-17 and steel was modeled using 2 zones across the 0.8 mm thickness. The 203.2 mm nominal length of the high explosive filled steel cylinder was defined by 1120 mesh elements. Air surrounds the cylinder configuration at a diameter of 240 mm and extends 50 mm beyond the ends. The air is represented in the computational mesh by 160 elements defining the diameter and 1280 mesh elements defining the total length of 303.2 mm.

The size of the mesh elements may alter the calculated solution. Due to that, careful creation of hexahedral zones with 1:1:1 aspect ratio produces the 80 million-element computation mesh.

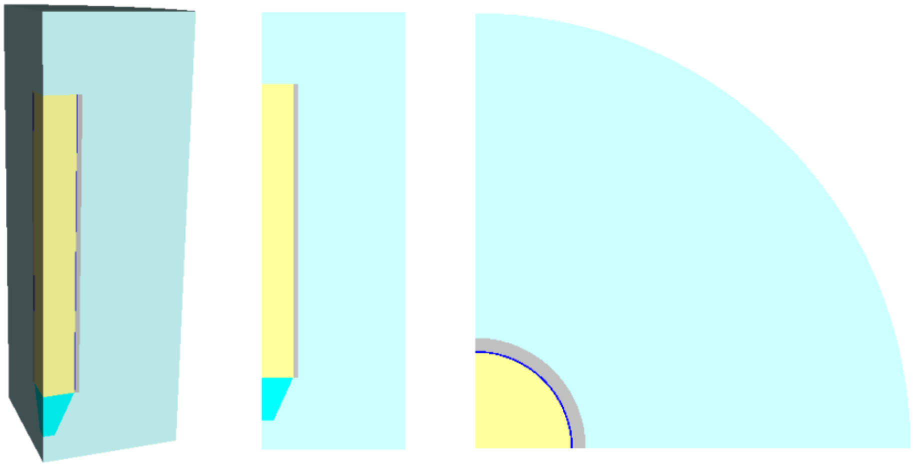

Figure 7 - Simulations images of the cylinder configurations. 3D quarter geometry is left, a 2D slice is middle and a top view looking down the length of the cylinder is right. Light blue represents the air, gray is the steel cylinder, dark blue is the thin silastic layer, light yellow is the LX-17 main charge and cyan is the LX-10 booster charge which is located on the detonating end of the cylinder configuration.

The LX-10 frustum booster is "shaped" over the air at the detonating end of the cylinder. The use of shapes simplifies the meshing process for complex geometries but creates mixed zones of LX-10 high explosive and air at the start of the simulation. The specification of mixed zones does not affect the fracture behavior of the steel, which occurs later in time. Detonation of the booster (and the start of the calculation) was initiated at the top center point of the LX-10 frustum. This "point detonation" approach simulates the function of the RP-1 detonator and initiates the program burn in the LX-10 booster charge. The purpose of the booster is to initiate a uniform detonation (in time) across the diameter of the LX-17 high explosive (main charge), igniting an augmented beta burn.

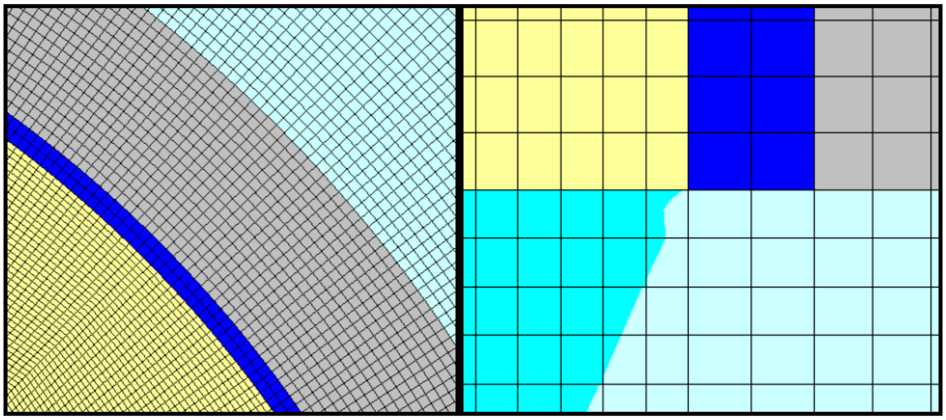

Figure 8 - 2D images of conformal meshing of the LX-17 (light yellow), silastic (dark blue), steel (gray) and air (light blue) interfaces (left) looking down the length of the cylinder from the detonated end and the mixed zones created by shaping in the LX-10 frustum (right).

In order to simplify the computational modeling of the cylinder, quarter symmetry was assumed. This required the specification of symmetry planes on the exposed internal faces of the cylinder configuration (refer to Figure 6, left). Outflow and pressure boundary conditions were specified at the outer (quarter) geometric edges of the air boundary.

Results and Discussion

ALE Calculations with Void Seeding and Slide Surfaces

Figure 9 is an ALE calculation result illustrating material fracture (separation) using the void seeding technique. The image corresponds to 24 μs, at which time approximately 80% of the LX-17 has detonated. At the top of the image, fractured steel (gray) and void (yellow) is observed. Zones that represent the steel were modeled as Lagrangian until the high explosive (LX-17) burn was complete, which occurs approximately 30 μs in the simulation. The steel zones were then allowed to advect to accommodate mesh distortion and avoid mesh tangling. The detonation and rapid expansion of the steel caused by the LX-10 booster at the detonating end of the cylinder causes significant mesh distortion, which advection is required to relax or remap to avoid Lagrangian mesh tangling. Similar mesh management is also required at the bottom end of the cylinder due to rapid expansion of the air surrounding the cylinder configuration and the mesh distortion caused by the LX-17 detonation. Ideally, the steel mesh remains Lagrangian throughout the duration of the problem to ensure accuracy of the solution; however, the dynamic behavior of the detonation can activate early advection. In an attempt to avoid early advection, restrictions on the distortion and velocity of the steel mesh elements were defined. When a zone distorted 95% from its original mapping or reached an improbable velocity of 4 km/sec (unlikely considering the highest velocity recorded was approximately 1.5 km/sec) could the steel zone advect to avoid mesh tangling.

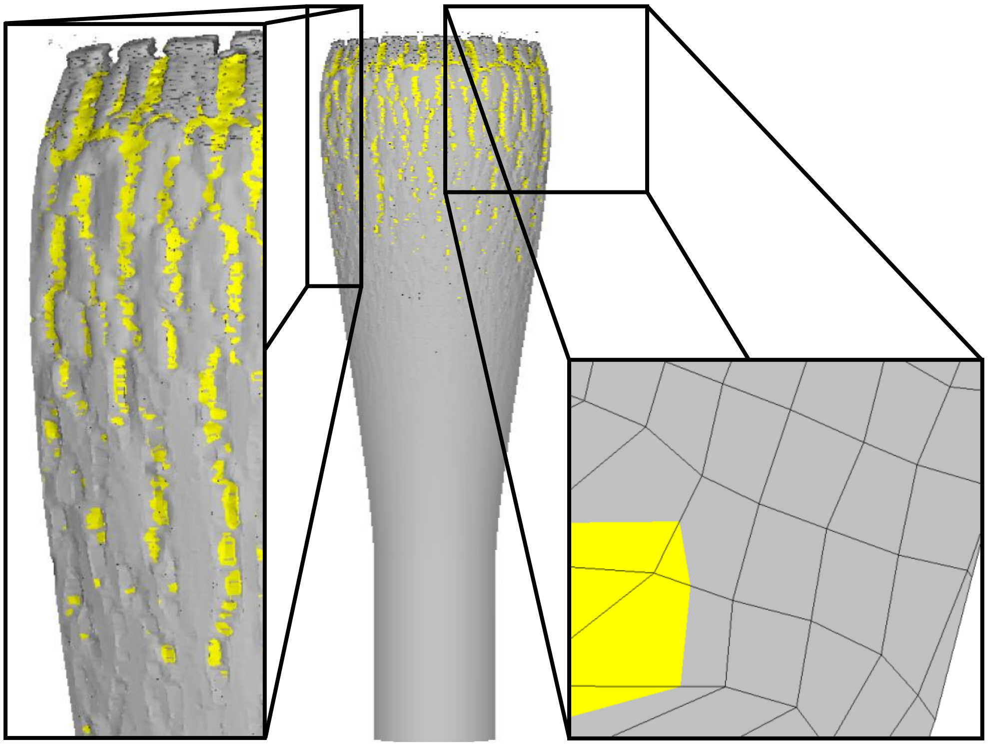

Figure 9 - 3D simulation image of fractured steel (gray) and void (yellow) (left) at time 24 μs and 2D slice (right) showing mixed zone formulation. Void seeding is often used to create visual fracture and fragmentation patterns in ALE simulations.

Embedded Grid Calculations with Element Erosion

Figure 10 is a two-dimensional slice of the three-dimensional embedded grid calculation result illustrating material fracture (separation) using the element erosion technique. The image corresponds to 24 μs, at which time approximately 80% of the LX-17 has detonated. The two images of the steel (gray) are representative of approximately 50 mm from the detonating end of the cylinder. The steel zones in the foreground mesh are modeled Lagrange for the duration of the simulation. If a zone becomes 95% distorted from its original hexahedral (1:1:1 aspect ratio) mapping and accumulates 98% damage, the zone is deleted to avoid mesh tangling. Figure 10 illustrates the eroding of two steel zones that reached the specified criteria to delete from the 24 μs to 25 μs time step.

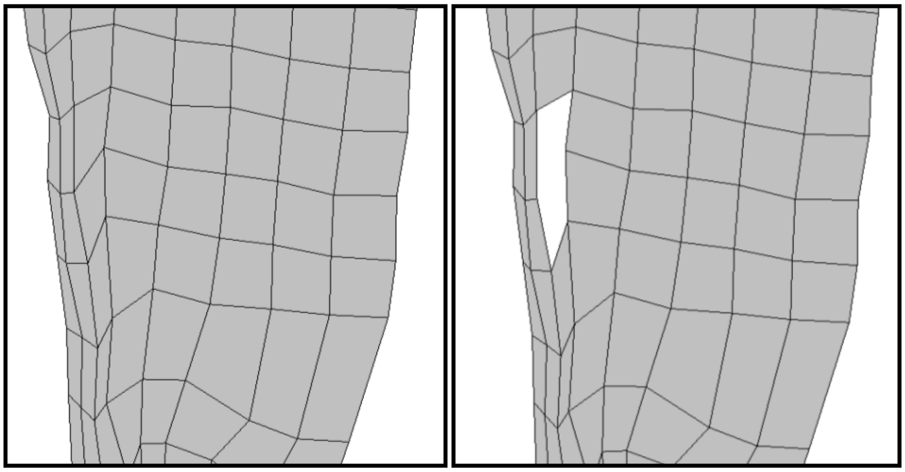

Figure 10 - 2D simulations images detailing element erosion, two steel (gray) elements were deleted between the two plot files (24 μs to 25 μs) due to the distortion and damage criteria.

Mass Conservation of ALE and Embedded Grid Modeling Approaches

Mass deletion from the eroded steel zones defined in the embedded grid approach requires further investigation. Ideally, in the computational simulations 100% of the mass is retained. This occurs in the ALE calculations (Figure 11, left). However, by using element erosion, if all elements surrounding a node reach the deletion criteria and erode, the mass associated with that node (and its contributing eroded elements) will be deleted. The mass for the steel region was plotted for the duration of the simulation for the ALE and embedded grid approaches. The embedded grid calculations deleted approximately 3 g, which is 1.65%. The embedded grid calculations retained 98.4% of the original 180 g mass.

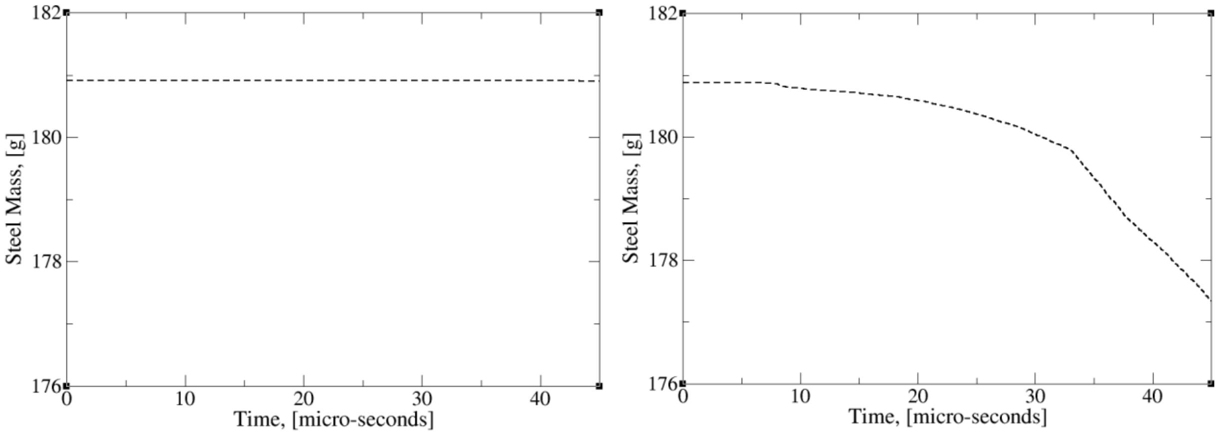

Figure 11 - Tracking the steel mass throughout the duration of the ALE (left) and embedded grid (right) simulations, zoomed in perspective of 176 g to 182 g to depict the mass loss of element erosion (right).

Statistical Sampling of the Weibull Distribution for Mesh Convergence Study

To accurately reproduce the statistical distribution of the Johnson-Cook damage parameter, D_2, the computational models required a sufficient sampling of the cumulative Weibull distribution function (refer to Figure 5). A sufficient number of sample points was determined by increasing the number of samples through increasing the spatial density of zones in the calculation. If more steel zones are present within the simulation, the more sampled D_2 values are seeded, thusly more accurately reproducing the Weibull distribution (Figure 5) at the start of the simulation. The smoothness of the first derivative of the number of zones seeded with the corresponding D_2 value was used as the convergence criterion. The derivative was normalized within its data set to compare different mesh resolutions. The number of mesh elements spanning the 3 mm steel cylinder thickness defined the mesh resolution.

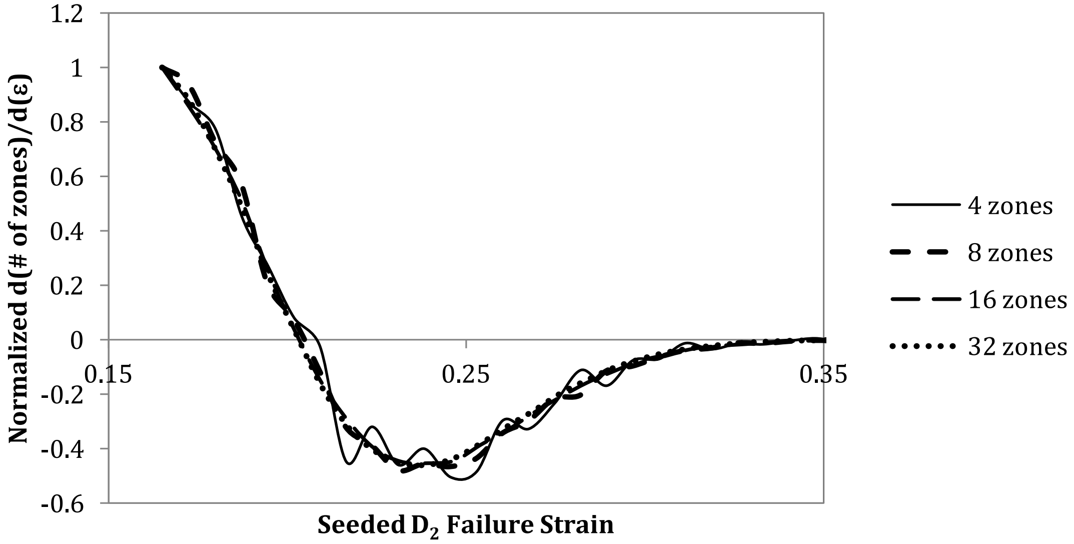

Figure 12 - Mesh convergence study from the ALE modeling approach investigating the statistical seeded D_2 Johnson-Cook damage coefficient. A derivative was taken of the amount of zones seeded with a specific D_2 value and normalized to compare the smoothness of 4, 8, 16 and 32 mesh zones across the 3 mm steel thickness.

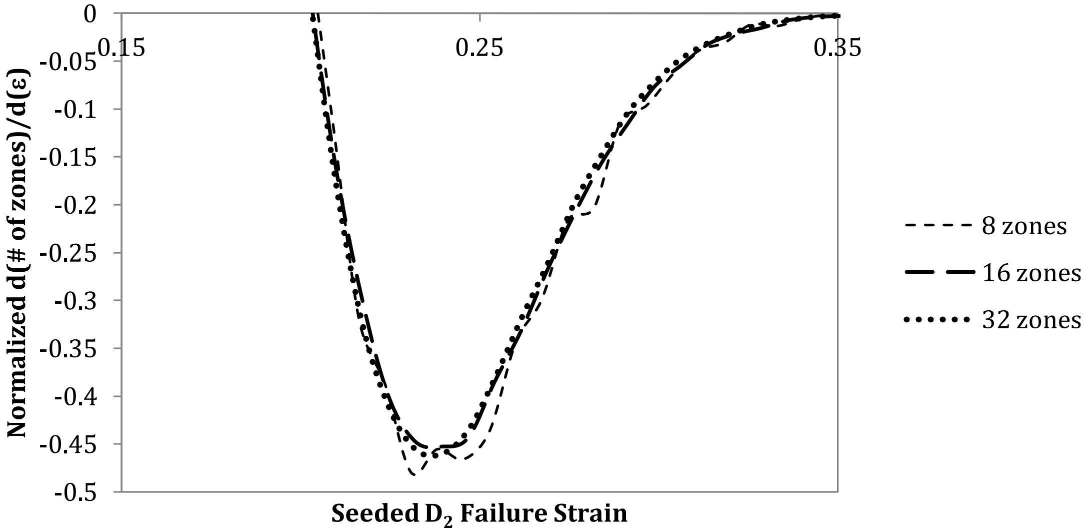

Figure 13 - Zoomed in perspective of the mesh convergence study from the ALE modeling approach looking at 8, 16 and 32 square mesh elements across the steel thickness.

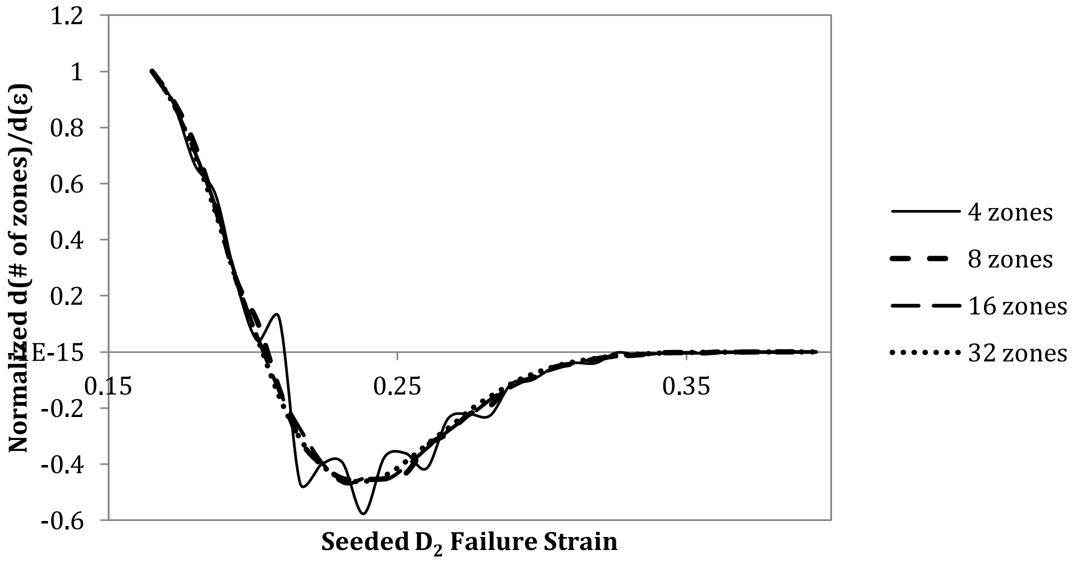

Figure 14 - Mesh convergence study from the embedded modeling approach investigating the statistical seeded D_2 Johnson-Cook damage coefficient. A derivative was taken of the amount of zones seeded with a specific D_2 value and normalized to compare the smoothness of 4, 8, 16 and 32 mesh zones across the 3 mm steel thickness.

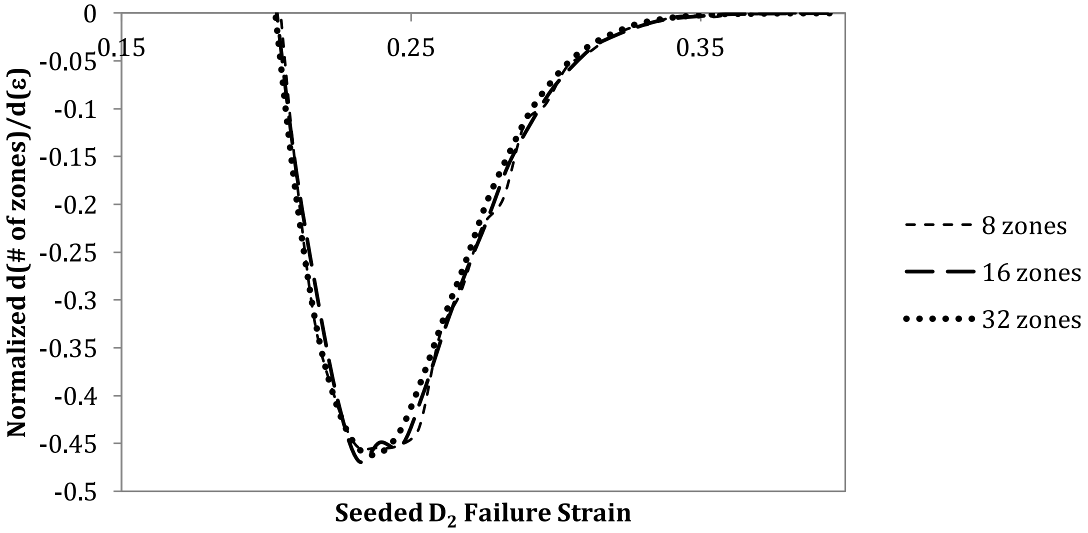

Figure 15 - Zoomed in perspective of the mesh convergence study from the embedded grid modeling approach looking at 8, 16 and 32 square mesh elements across the steel thickness.

The results indicate that a computational mesh characterized by 16 zones spanning the 3 mm steel thickness is sufficient to accurately represent the (input) Weibull distribution defined by the measured failure strains for ALE and embedded grid modeling approaches.

Verifying Steel Expansion Velocity (Velocimetry)

A mesh convergence study on the cylinder expansion rate suggests that the current computational mesh is converged. In addition, the study suggests the cylinder expansion rate is insensitive to mesh refinement over the range of mesh resolutions evaluated. The calculated results were in relatively good agreement with the measured cylinder expansion (velocimetry) data after applying a time shift (+2.75 μs) to account for the RP-1 detonator used in the actual experiment. The initial acceleration (jump off) suggests that the high explosive shock has propagated to the (outer free) steel surface. The abrupt deceleration (pull back) is due to the shock reflection at the free surface and the subsequent acceleration results from the internal pressure created by the expanding high explosive reaction products (gas). The measured velocimetry curves terminate due to the expansion of the high explosive reaction products (i.e. smoke) which obscures the probes' laser line of sight. The ALE and embedded grid simulations accurately calculate the intervals between subsequent jump-off signals measured during the experiment (in 4 to 5 μs intervals). Both modeling approaches calculate a higher velocity at initial jump off and a lower velocity at pull back. These differences may be associated with low data resolution from the processing and analysis of the measured raw data [9].

The ALE and embedded grid calculations are in good agreement with the measured data to calculate initial jump off and pull back of the steel. The ALE and embedded grid calculations deviate when the fractured cylinder accelerates after pull back. The calculation results trend toward lower cylinder expansion velocities at later times (approximately 5 to 10 μs after pull back is calculated for each probe). The measured data exceed 1.5 km/s and approach an expansion velocity of 1.75 km/s whereas the ALE calculations approach 1.6 km/s and the embedded grid calculations approach 1.5 km/sec. These lower velocities may be the result of calculated material failure (as a result of using the Johnson-Cook failure model). Cracking and fracture of the steel cylinder release the internal pressure, resulting in a reduction of energy and applied force on the fractured steel. The embedded grid approach calculates lower velocities compared to the measured data and the ALE calculations. This could be a result of the use of element erosion in the embedded grid approach. Due to potential mass loss from the deletion of elements, the resulting velocity may be reduced. Element erosion could vent (and consequently reduce) the internal pressure through the fractured steel. A sudden decrease in velocity is calculated at late time (40 μs) in the ALE approach. This decrease is not present within the experimental data and can be attributed to the use of advection (mesh relaxation) in the ALE calculations. Ideally, the steel casing is modeled as Lagrangian for the duration of the simulation. In reality, however, the cylinder is Lagrangian until complete detonation of the LX-17 main charge, which occurs at 30 μs. As advection occurs, the steel zones relax and the calculated velocity is no longer a reliable measurement of the steel cylinder expansion. This is depicted by the velocity of the first probe (P1) at late time (40 μs) in Figure 16, left.

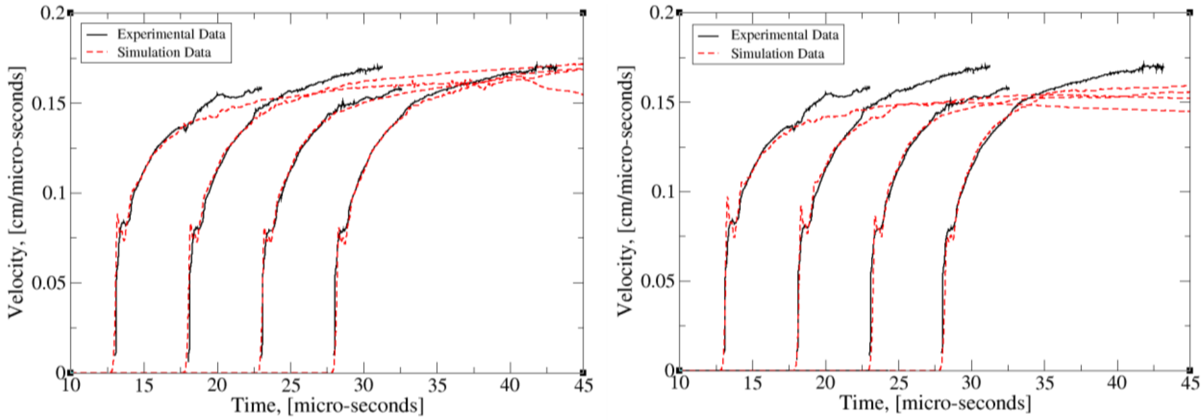

Figure 16 - Experimentally measured (black) and simulation calculated (red dotted) cylinder expansion velocity, from ALE (left) and embedded grid (right). Simulations depicted here have Steinberg-Guinan strength and a statistics compensated Johnson-Cook failure model.

Evaluating the Global Deformation of the Cylinder

Due to the different approaches to introduce material failure into the computational mesh (void seeding with ALE calculations and element erosion for embedded grid calculations), the visual fracture patterns differ in appearance. The fracture patterns are more distinguishable in the embedded grid approach as compared to the ALE approach. The simulations were visualized by plotting the failure (according to Johnson-Cook) and restricting the view to un-failed material, denoted by the dark blue color. The variable of failure is visualized as a flag with un-failed material having a value of zero (dark blue visualized) and failed material represented with a value of 1.0 (red, not visualized). This yields a simulated fracture pattern for each approach, which can be visually compared to the experimental image (given in Figure 2). Below is the evolution of steel failure in the ALE (Figure 17) and embedded grid (Figure 18) simulations at time, t = 20, 30, 40 and 50 μs.

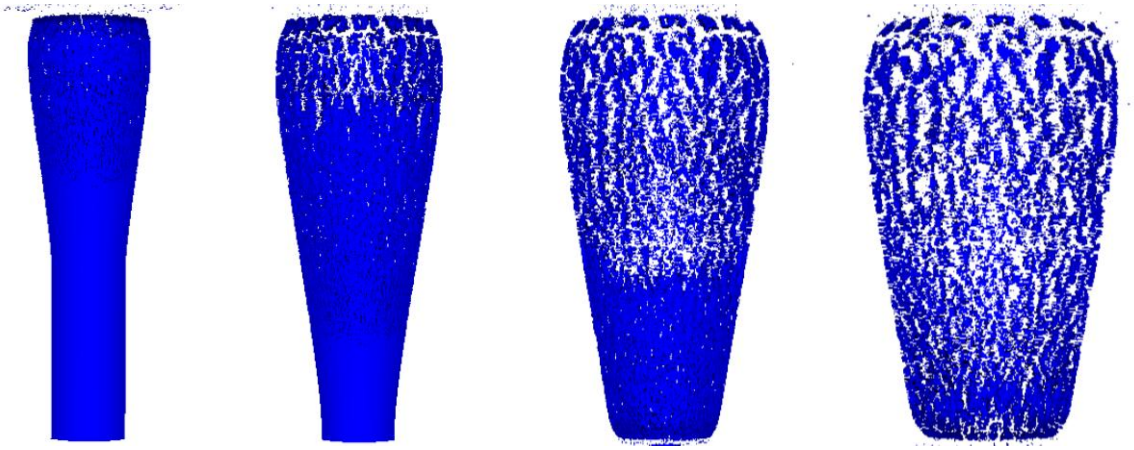

Figure 17 - Evolution of fracture according to the ALE calculations. Simulation images correspond to 20, 30, 40 and 50 μs. Fracture is visualized by a threshold restricting the view to un-failed steel zones (denoted by dark blue).

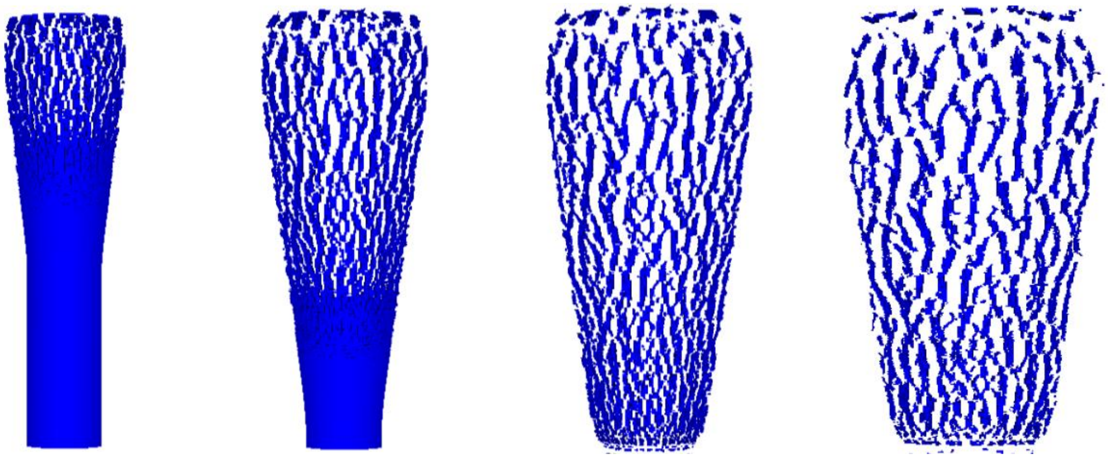

Figure 18 - Evolution of fracture according to the embedded grid calculations. Simulation images correspond to 20, 30, 40 and 50 μs. Fracture is visualized by a threshold restricting the view to un-failed steel zones (denoted by dark blue).

The visual differences compare the two methods utilized to calculate steel fracture. The "fragments" appear to be longer and more slender in the embedded grid approach as compared to the wider "fragments" calculated by the ALE approach. Further analysis of the fracture pattern was achieved with comparisons to experimental high-speed digital framing camera images.

High-speed digital framing cameras provide 1 μs inter-frame visual images of the detonation. Figure 19 is a snapshot in time (t = 21 μs) that illustrates all aspects of the cylinder's response to high explosive detonation. Dynamic fracture and fragmentation is evident at the top of the cylinder, concluded by the appearance of high explosive reaction products (smoke) venting through the cracked steel. The middle of the cylinder is fractured (deformation caused by the rapidly expanding detonation products) but not yet failed (cracked) to release the smoke. At this time, the detonation has yet to reach the bottom of the cylinder based on its un-deformed shape. A mesh convergence study on the visual cylinder expansion (fracture pattern) suggests that the current computational mesh is converged. In addition, the study suggests the visual cylinder expansion (fracture pattern) is insensitive to mesh refinement over the range of mesh resolutions evaluated.

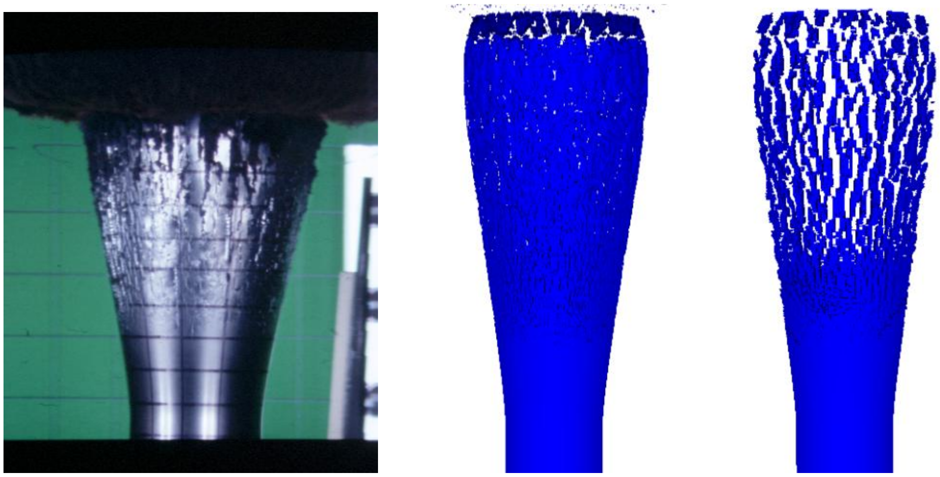

Figure 19 - Comparison of visual material failure of experimental high speed camera image (left), ALE calculations (middle) and embedded grid calculations (right). The simulations are visualized with a threshold which restricts the view to only un-failed (denoted by dark blue) zones.

The Taylor angle is a convenient metric by which to compare the calculated and measured cylinder expansion behavior. It is defined as the angle between the expanded portion of the cylinder and the un-expanded portion. The Taylor angle can also be determined by the ratio of the velocities of the expanding cylinder and the detonation, defined in [3]:

$$\frac{V.O.F.}{V.O.D.} = 2sin\frac{1}{2}\theta \qquad (14)$$

where *V.O.F.* is the velocity of fragment (or cylinder wall), *V.O.D.* is the velocity of detonation (detonation velocity of LX-17), and θ is the Taylor angle. Due to the detonation occurring at one end, the cylinder will expand in a cone shaped geometry, producing a measured Taylor angle of 14° [10]. In comparison, an angle of expansion of 10° was measured from the computational simulations, based on the geometry at comparable simulation time[1]. Using equation 14, the approximate Taylor angle is measured to be 11.4°, by:

$$\sin^{-1}\left[\frac{1.5\ mm/\mu s}{2*7.596\ mm/\mu s}\right] = \frac{1}{2}\theta = 5.7°$$

---

[1] Using t = 24 μs, after applying a time shift to account for the RP-1 detonator. This shift describes the time difference between the experiment and the simulations.

where the asymptotic value of the expansion rate for the cylinder is 1.5 mm/μs (Figure 14) and the detonation velocity for LX-17 is 7.596 mm/μs [15]. Both estimates are in relatively good agreement with the measured value of 14°.

Verifying Stress State (Stress Triaxiality Ratio)

The stress state of an experimental configuration can be related to the stress triaxiality ratio, which is often used to characterize the severity of the multi-axial tensile stress state in a fracture model. Therefore, the stress state for the cylinder was analytically derived by assuming plane strain loading conditions. The analytical derivation is compared to the code calculated stress state for the cylinder simulations. The stress triaxiality ratio is a non-dimensional stress and is defined as the ratio of the von Mises stress to the mean (average) stress:

$$\bar{\sigma} = \sqrt{\frac{1}{2}[(\sigma_1 - \sigma_2)^2 + (\sigma_2 - \sigma_3)^2 + (\sigma_3 - \sigma_1)^2]} = \sqrt{J_2} \qquad (15)$$

$$\sigma_m = \frac{\sigma_1 + \sigma_2 + \sigma_3}{3} = \frac{1}{3} I_1 \qquad (16)$$

where $\bar{\sigma}$ is the von Mises stress (square root of J_2) and σ_m is the mean stress (average stress or $I_1/3$). A radially expanded cylinder is assumed to be plane strain, and from the work of Hancock and Mackenzie [12], $\sigma_1 = 2\sigma_2$ and $\sigma_3 = 0$. The mean stress can therefore be written as:

$$\sigma_M = \frac{1}{3}\left(\sigma_1 + \frac{1}{2}\sigma_1\right) = \boldsymbol{\frac{1}{2}\sigma_1}$$

and the von Mises stress is:

$$\bar{\sigma} = \sqrt{\frac{1}{2}[\left(\sigma_1 - \frac{1}{2}\sigma_1\right)^2 + \left(\frac{1}{2}\sigma_1 - 0\right)^2 + (0 - \sigma_1)^2]}$$

$$= \sqrt{\frac{1}{2}\left(\frac{1}{2}\sigma_1\right)^2 + \left(\frac{1}{2}\sigma_1\right)^2 + (\sigma_1)^2} = \sqrt{\frac{1}{2}\left(\frac{3}{2}(\,\sigma_1)^2\right)} = \boldsymbol{\frac{\sqrt{3}}{2}\sigma_1}$$

The stress triaxiality ratio for the cylinder is defined as $\frac{\sigma_M}{\bar{\sigma}} = {}^{\frac{1}{2}\sigma_1}\Big/_{\frac{\sqrt{3}}{2}\sigma_1} = \boldsymbol{\frac{1}{\sqrt{3}}}$ or **0.577**. This value is compared to the asymptotic behavior computed by the simulations. The stress triaxiality computed by ALE3D varied, as a result of the dynamic nature of the problem and the propagation of stress waves throughout the steel material. The stress triaxiality ratio within the steel cylinder was estimated by tracking the (stress over strain) loading history of a small volume of material centered within the cylinder thickness, approximately 38.1 mm from the end of the cylinder. A mesh convergence study on the stress triaxiality ratio indicated that the current computational mesh is converged and that it is insensitive to mesh resolution. Results are illustrated below.

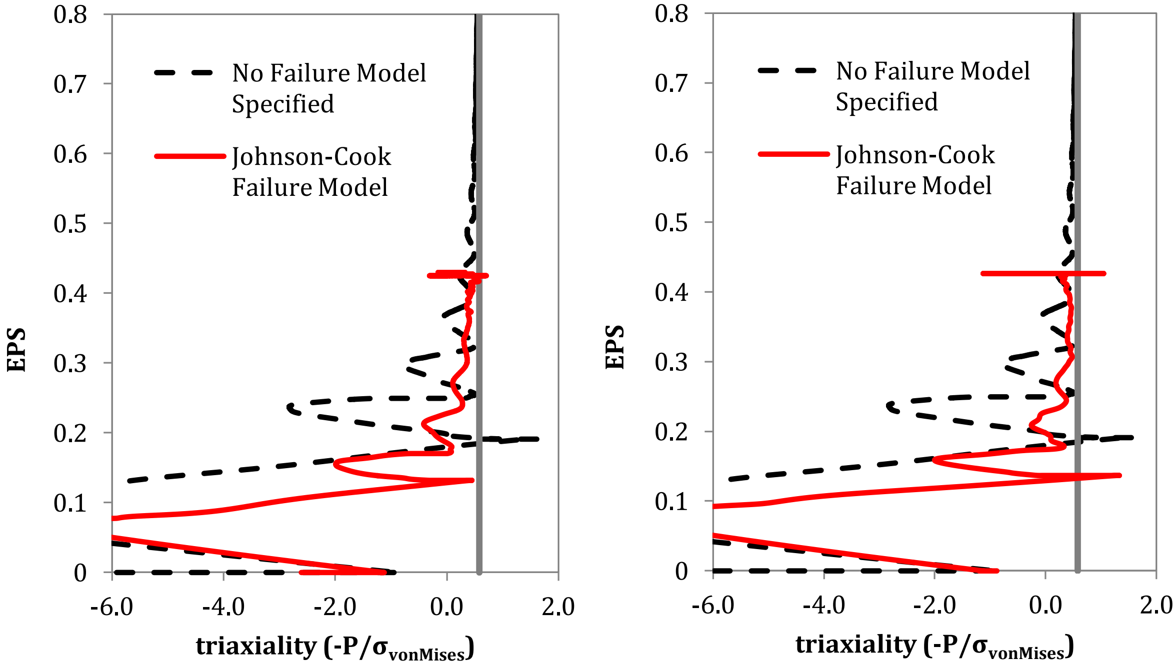

Figure 20 - Simulation calculated EPS as a function of triaxial stress. Positive triaxiality denotes a tensile stress state. If a failure model was not specified, this behavior would continue to trend towards the analytical values as shown by the black dotted lines.

The figures illustrate that the mechanical response of the small volume of material as it asymptotically approaches the derived analytic stress triaxiality ratio value of 0.577. The response follows a period of oscillations in which high pressure stress propagation within the material dominate the response. Since both computational methodologies use the Johnson-Cook failure model, failure occurred (at approximately 40% EPS) before the oscillations could fully asymptote to 0.557 (shown by the red solid lines in Figure 17). Any deviation from the analytical loading conditions value as calculated by the simulations could be the result of the experimental loading conditions representing some divergence from plane strain.

Evaluating the Statistics Compensated Johnson-Cook Failure Model

The Johnson-Cook failure model is defined by the accumulation of damage, which can be related to the accumulation of strain of a zone. Once a zone has accumulated damage = 1.0 and fails, it cannot amass additional strain. Due to the inherent statistical nature of material failure, as shown by the distribution of recovered fragments and their corresponding measured failure strain, it can be assumed that statistical variation will be observed in the equivalent plastic strain (EPS) distributions before and at the time of failure.

Evaluating Fracture in the Expanded Steel Cylinder using Average EPS

The EPS in the steel region (including both failed and un-failed zones) is illustrated in Figure 21, as a function of time. The average EPS value increases linearly with increasing time and plateaus at approximately 40 μs. A mesh convergence study on the average EPS for the steel indicated that the current computational mesh is converged for the range of resolutions evaluated, even though it is more sensitive to mesh refinement. Results are illustrated below.

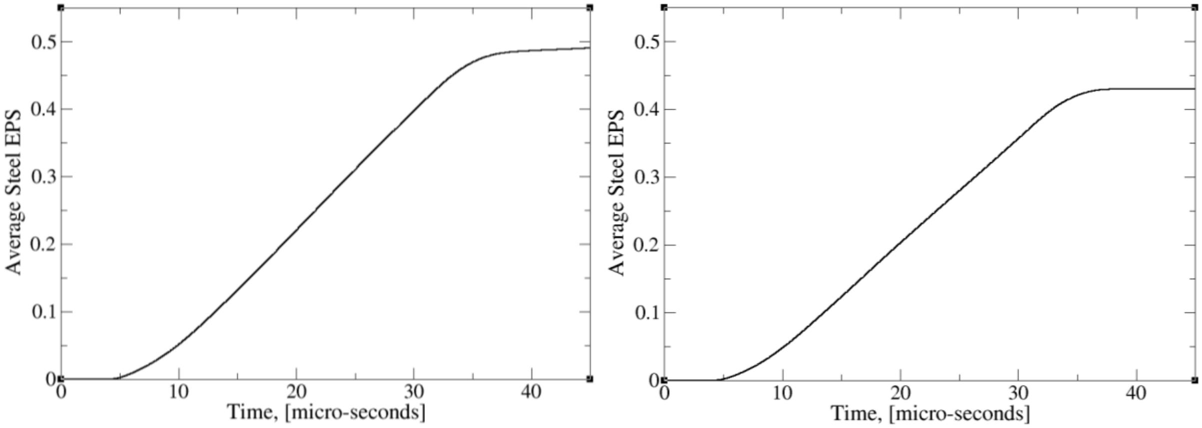

Figure 21 - Plots of average steel EPS for ALE calculations (left) and embedded grid calculations (right).

The embedded grid approach calculates a lower EPS at time of plateau. This would suggest the steel is failing at a lower EPS in the embedded grid calculations as compared to the ALE calculations. The difference in the EPS of the two modeling approaches could be attributed to the use of void seeding with the ALE approach and element erosion with the embedded grid approach. At the time of plateau (40 ms), the LX-17 main charge has completely detonated (30 μs to burn through main charge), and the fractured steel is propagating radially outwards. It can be assumed that the steel cylinder has largely ceased plastically deforming since the average EPS is no longer rapidly increasing (i.e. complete cylinder fracture has been achieved). Due to this assumption, the EPS of the failed steel material will be investigated at t_{final} = 40 μs (complete fracture), $t_{3/4\text{-}time}$ = 30 μs (complete detonation) and $t_{1/2\text{-}time}$ = 20 μs (detonation is approximately 120 mm from the detonating end of the cylinder) for statistical variation. To study the EPS of the failed zones, the use of thresholds restricted the distributions to reflect zones with accumulated Johnson-Cook damage of greater than 1.0.

Statistical Variation in the EPS of Failed Steel Zones

The EPS distributions were created by plotting the number of failed zones exhibiting a specific EPS (using 32 bins for uniformity) and superimposing Gaussian distributions to classify the statistical variation. A mesh convergence study on the EPS distributions for the failed steel zones indicated that the current computational mesh is converged for the range of resolutions evaluated, even though it is more sensitive to mesh refinement. Results are illustrated below.

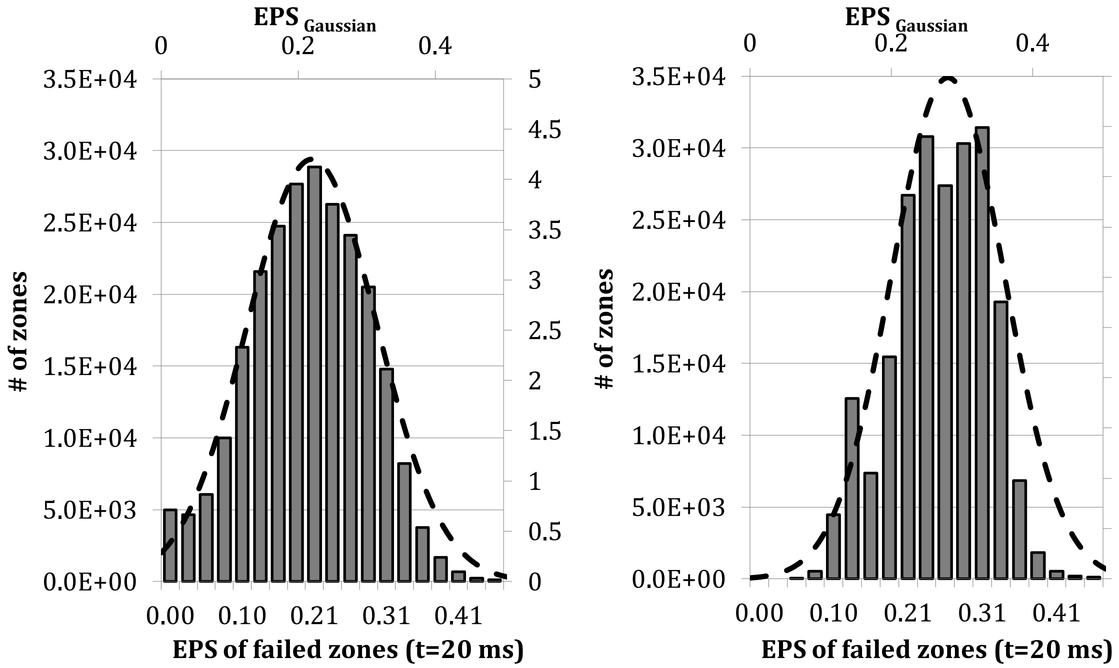

Figure 22 - EPS distribution with superimposed Gaussian curve for failed steel zones at t = 20 μs for the ALE (left) and embedded grid (right) calculations. The failed zones are defined by exceeding the Johnson-Cook damage accumulation criteria (D > 1.0).

The appearance of failed zones at 20 μs indicate material failure in the steel. The EPS distributions of the failed zones at 20 μs appear to be Gaussian with an arithmetic average strain of 0.21 for the ALE calculations and 0.26 for the embedded grid calculations. The ALE and embedded grid approach calculate EPS distributions at 20 μs with visible differences (as compared to each other). The shape of each distribution is related to the method of calculating steel failure in each modeling approach (void seeding for ALE calculations and element erosion for embedded grid approach). However, both approaches indicate that the EPS distributions at 20 μs exhibit Gaussian behavior.

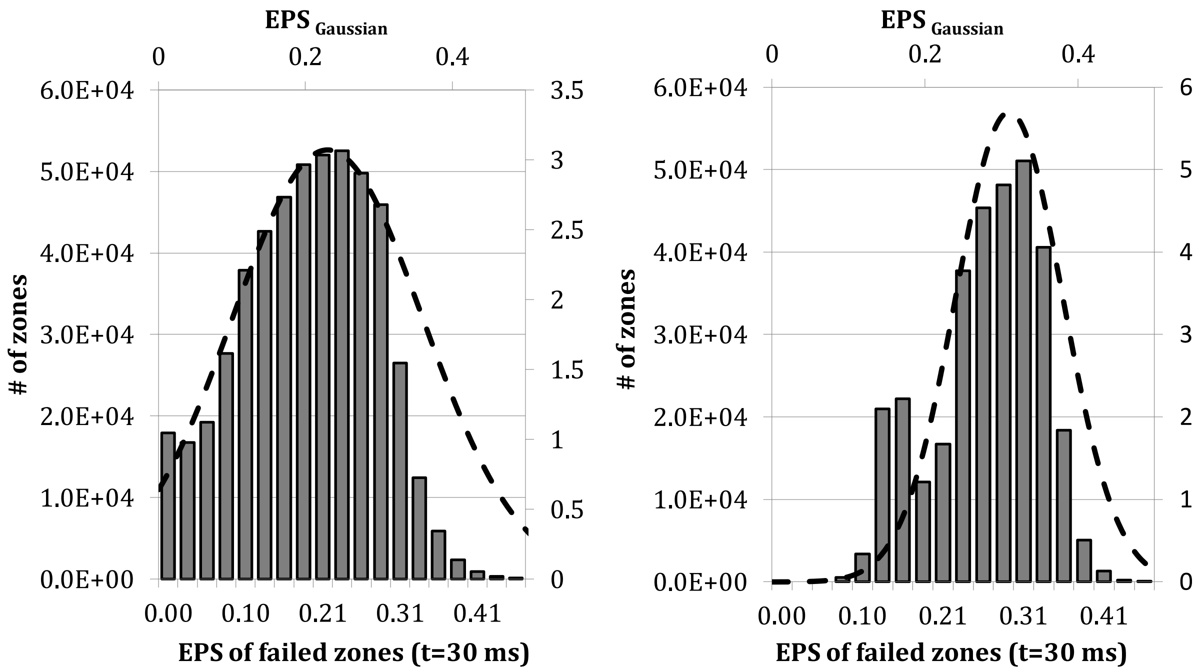

Figure 23 - EPS distribution with superimposed Gaussian curve for failed steel zones at t = 30 μs for the ALE (left) and embedded grid (right) calculations. The failed zones are defined by exceeding the Johnson-Cook damage accumulation criteria (D > 1.0).

The EPS distributions of the failed zones at 30 μs continue to exhibit Gaussian behavior with an arithmetic average strain of 0.26 for the ALE calculations and 0.28 for the embedded grid calculations. Again, the shape of the EPS distribution differs for each modeling approach. More data is present in the range of zero EPS to the average (0.26) than from the average to 1.0 EPS for the ALE calculations. At 30 μs, advection may be occurring (at the top or bottom of the cylinder to avoid mesh tangling) in the steel zones of the ALE calculations, which could affect the EPS distribution (Figure 23, left).

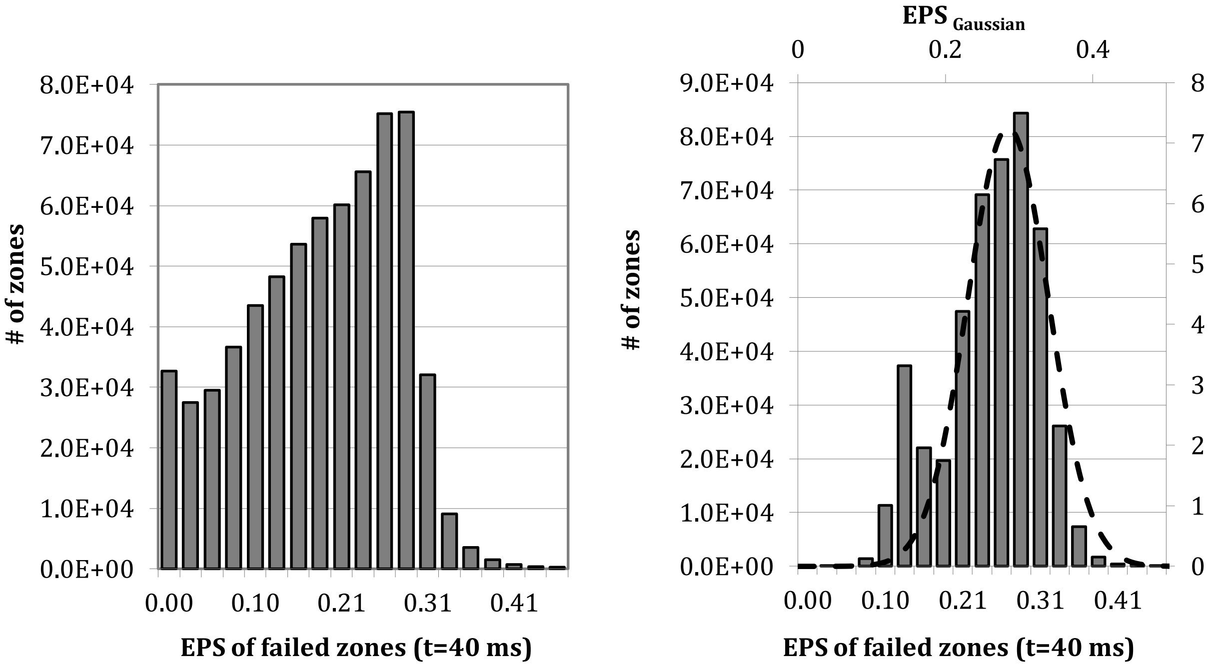

Figure 24 - EPS distribution with superimposed Gaussian curve for failed steel zones at t = 40 μs for the ALE (left) and embedded grid (right) calculations. The failed zones are defined by exceeding the Johnson-Cook damage accumulation criteria (D > 1.0).

The EPS distributions for failed steel zones at 40 μs show variation between the ALE and embedded grid simulations techniques. The embedded grid calculations exhibit Gaussian behavior with an arithmetic average of 0.28. The ALE calculations do not exhibit Gaussian behavior at 40 μs of the failed zones. The most likely cause of the lack of Gaussian behavior is advection. Due to the relaxation of the mesh, the EPS values for the advected steel zones are no longer reliable. Another potential cause for the behavior could be the use of void seeding. Once void is inserted into a steel zone, the steel zone is flagged as unfailed and could potentially continue to accumulate strain until damage equates to 1.0 again. Therefore, the amount of strain due to the zone failing more than once, could differ from the EPS when the zone fails once.

Conclusions and Summary

The objective of this study was to investigate the material failure of a hollow steel cylinder loaded with high explosive through ALE3D computational simulations. These computational simulations utilized the Steinberg-Guinan strength model for the steel response, the Mie-Grüneisen equation of state for the steel and the Jones-Wilkins-Lee equation of state for the LX-17 and LX-10 high explosive response. In addition, a statistics compensated Johnson-Cook failure model was utilized for the steel cylinder. The Johnson-Cook failure model was statistically compensated with a Weibull distribution derived from the measured strain to failure of the recovered steel fragments from the experiment. Material failure of the steel cylinder was modeled in two approaches, ALE with void seeding and embedded grid with element erosion. The simulation calculations of ALE and embedded grid were compared to experimental data of a cylinder experiment described in [10] for model verification through the metrics of mass conservation, velocity of steel expansion, global deformation and fracture pattern, stress triaxiality behavior and the statistical variation exhibited by the equivalent plastic strains (EPS) of the failed steel zones.

By using a multi-physics code (ALE3D), a statistics compensated Johnson-Cook failure model will simulate fracture patterns and distributions of strain relatively similar to the observed results of the experiment. This similarity is observed for both modeling approaches of ALE and embedded grid. However, since both approaches are only approximations to calculating material failure, differences in the comparison metrics are present.

By further investigating the embedded grid approach through a computational mesh refinement study, the background and foreground mesh may be better coupled. This may decrease the amount of mass deleted from the embedded grid simulations with element erosion, and consequently decrease the amount of energy loss exhibited by the steel cylinder. Advection constraints can be further investigated to ensure advection does not interfere with the ALE calculations of material failure. Other future work may include the investigation of the un-failed zones for both approaches, in an attempt to examine the strain to failure (EPS) displayed by a "fragment" (consisting of un-failed steel zones).

References

[1] "AerMet® 100 Alloy." *AerMet® 100 Alloy*. N.p., n.d. Web. 08 Oct. 2015. <http://cartech.ides.com/datasheet.aspx?i=101&e=161&c>.

[2] ALE3D, T. (2014). ALE3D users manual, An Arbitrary La- grangian/Eulerian 2D and 3D Code System. Technical Report LLNL- SM-650174 - Version 4.22.x, Lawrence Livermore National Laboratory.

[3] Batchelor, G. K., F.R.S., ed. "The Scientific Papers of G. I. Taylor. Vol. III. Aerodynamics and the Mechanics of Projectiles and Explosions. Edited by G. K. B ATCHELOR . Cambridge University Press, 1963. 559 Pp. £5 or $17.50." *J. Fluid Mech. Journal of Fluid Mechanics* 17.04 (1963): 277-86. Print.

[4] Dobratz, B. M., and P. C. Crawford. "Properties of Chemical Explosives and Explosive Simulants." *LLNL Explosives Handbook* (1985): n. pag. Web.

[5] "Dow Corning Cookie Policy." *SILASTIC® MEDICAL ADHESIVE SILICONE, TYPE A*. N.p., n.d. Web. 15 Oct. 2015.

[6] Durrenberger, J., J. Florando, N. Barton, A. Attia, P. Norquist, and M. Tang. "Matprop Material and Model Listing for Midas Version 1.0." *Lawrence Livermore National Laboratory* (2011): n. pag. Print.

[7] Garrison, W., & Moody, N. (1987). Ductile fracture. *Journal of Physics and Chemistry of Solids, 48*(11), 1035-1074.

[8] Goto, D. M. "Damage Coefficients for Johnson-Cook Failure Model." 20 Aug. 2015. Private Communication.

[9] Goto, D. M. "Experimental Velocimetry Time Resolution." 12 Aug. 2015. Private Communication.

[10] Goto, D. M., R. C. Becker, T. J. Orzechowski, H. K. Springer, A. J. Sunwoo, and C. K. Syn. "Investigation of the Fracture and Fragmentation of Explosively Driven Rings and Cylinders." N.p., n.d. Print.

[11] Gurson, A. (n.d.). Continuum Theory of Ductile Rupture by Void Nucleation and Growth: Part I—Yield Criteria and Flow Rules for Porous Ductile Media. Journal of Engineering Materials and Technology, 99(1), 2-2.

[12] Hancock, J.W. *and* Mackenzie, A.C. *(*1976*)*. On the Mechanisms of Ductile Failure in High Strength Steels Subjected to Multi-axial Stress States , *Journal of Mech. Phys. Solids*, 24*:* 147-169

[13] Johnson, Gordon R., and William H. Cook. "Fracture Characteristics of Three Metals Subjected to Various Strains, Strain Rates, Temperatures and Pressures." *Engineering Fracture Mechanics* 21.1 (1985): 31-48. Print.

[14] Mackenzie, A., Hancock, J., & Brown, D. (1977). On the influence of state of stress on ductile failure initiation in high strength steels. *Engineering Fracture Mechanics, 9*, 167-188.

[15] N.p., n.d. Web. <http://www.teledynerisi.com/0products/1ebw/page20.html>.

[16] Steinberg, D. J., S. G. Cochran, and M. W. Guinan. "A Constitutive Model for Metals Applicable at High-strain Rate." *A Constitutive Model for Metals Applicable at High-strain Rate*. N.p., n.d. Web. 17 Nov. 2015.

[17] "The Weibull Distribution." *ReliaWiki RSS*. N.p., n.d. Web. 11 Sept. 2015. <http://reliawiki.org/index.php/The_Weibull_Distribution>.

[18] (2013). ALE3D Web page. <https://wci.llnl.gov/simulation/computer-codes/ale3d>.

Appendix

Investigation of Statistics Compensated Johnson-Cook Failure Model

Once defining the unknown damage coefficient, D_2, as a statistical Weibull quantity, further investigation yielded the evolution or charge of the distribution over the duration of the ALE simulation. As D_2 is intended to represent a material property, this evolution was troublesome. The evolution of D_2 was observed for the cylinder ALE calculations at t = 0 μs and t = 20 μs. At 20 μs, the detonation wave is approximately in the middle of the cylinder nominal length. Advection was not expected to occur in the conformal steel mesh at this time.

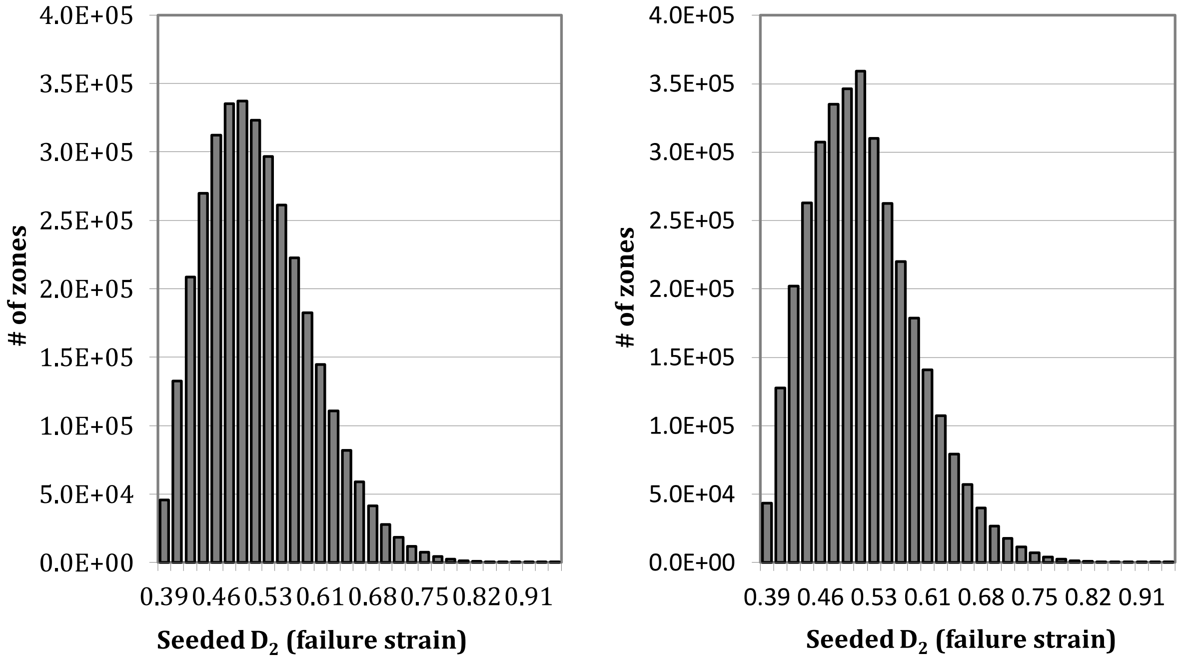

Figure 25 - Evolution of D_2 parameter at t = 0 μs (left) and 20 μs (right) for the ALE cylinder calculations. This evolution was unexpected.

Advection is a potential and probable cause for this behavior. Restricting the commands which control advection help the severity of the issue. Investigating this issue in the embedded grid approach resulted in the following figures. Negligible change is observed in the D_2 distribution from time, t = 0 and 20 μs, due to the Lagrangian foreground steel mesh where advection does not occur.

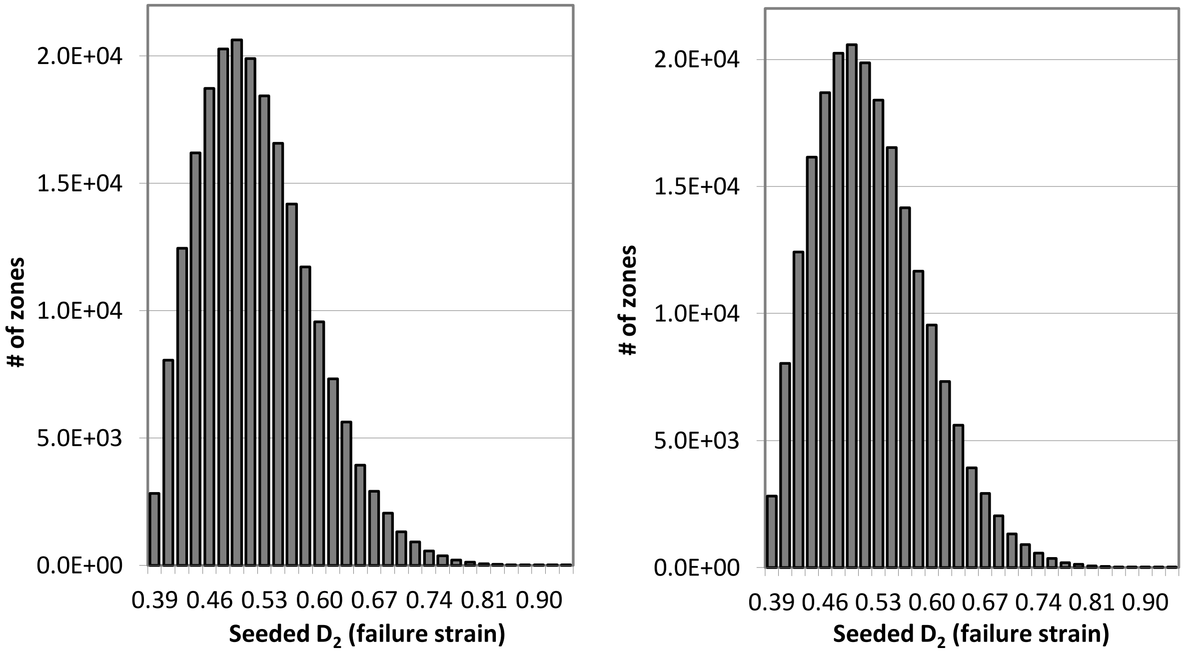

Figure 26 - Negligible evolution of the D_2 parameter at t = 0 μs (left) and 20 μs (right) for the embedded grid cylinder calculations.